Journal of Materials Chemistry A

Accepted Manuscript

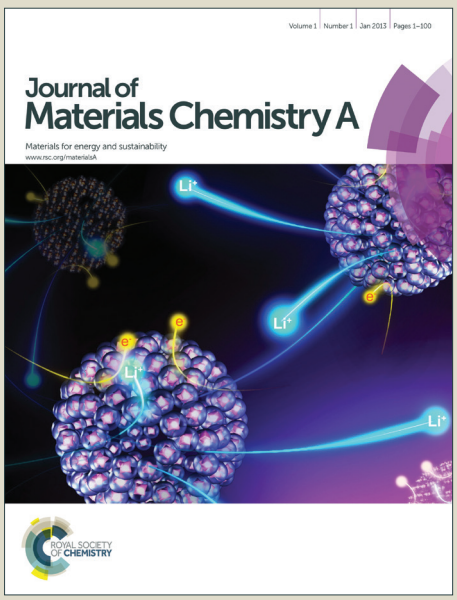

ROYAL SOCIETY OF CHEMISTRY

www.rsc.org/materialsA

Table of Contents

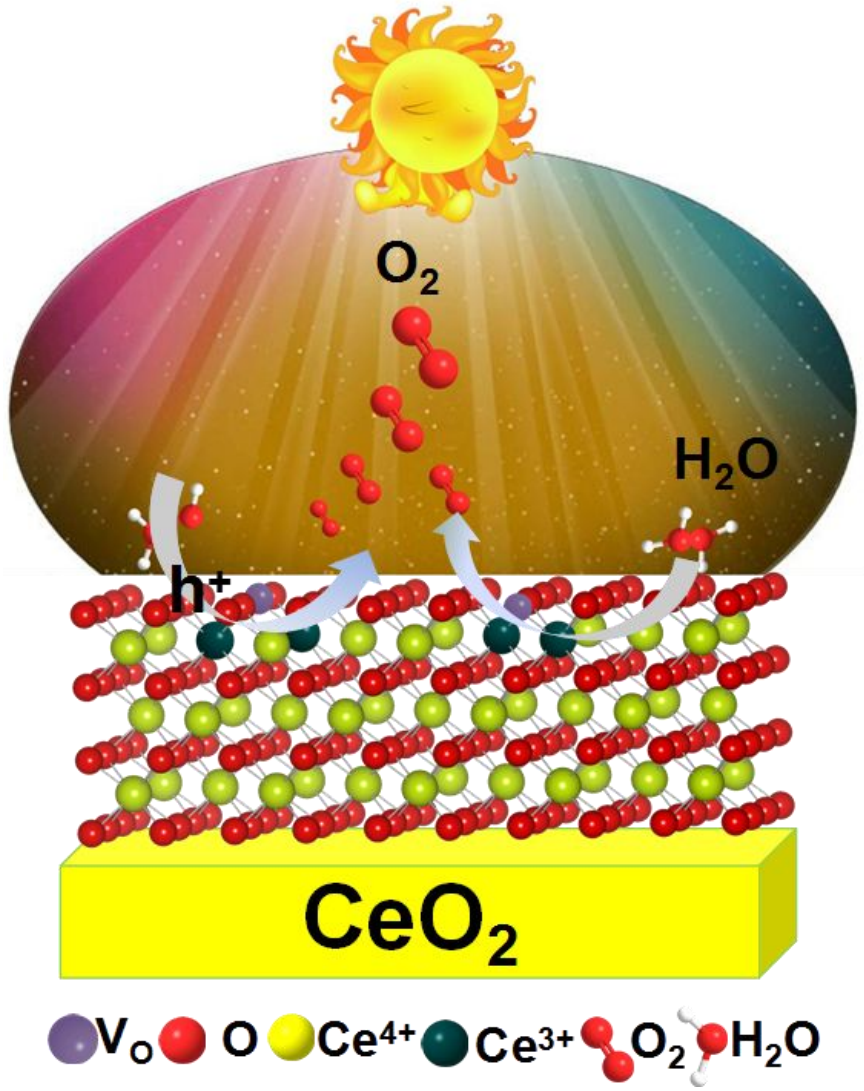

Surface defects including oxygen vacancies and Ce^{3+} ions on the surface of CeO_2 nanorods lead to an efficient catalytic activity towards water oxidation under visible light.

Journal of Material Chemistry A

COMMUNICATION

Efficient Water Oxidation under Visible Light by Tuning Surface Defects on Ceria Nanorods

Received 00th June 2015,
Accepted 00th July 2015

DOI: 10.1039/x0xx00000x

www.rsc.org/

Kun Zhao,[a,b] Jian Qi,[c] Huajie Yin,[b] Zumin Wang,[a] Shenlong Zhao,[b] Xiang Ma,[b] Jiawei Wan,[b] Lin Chang,[b] Yan Gao,*[b] Ranbo Yu*[a] and Zhiyong Tang*[b]

Fluorite CeO_2 nanorods (NRs) with tunable surface defects are successfully prepared via hydrothermal synthesis followed by post-calcination under different atmospheres. Impressively, the CeO_2 NRs obtained under mixed Ar and H_2 gas at 800°C exhibit superior catalytic activity towards water oxidation under visible light ($\lambda \geq 420$ nm), which is 10 times higher than that of CeO_2 NRs treated under air at 800°C. Detailed characterization and theoretical analysis reveal that the rich surface defects including surface oxygen vacancies and Ce^{3+} ions are the origin of the enhanced performance of water oxidation for the CeO_2 NRs treated under the reduced atmosphere.

Photocatalytic water splitting under irradiation of solar light is an intriguing approach to obtain renewable and clean energy for sustainable development in future.[1-3] Among many types of photocatalysts, transition metal oxide semiconductors have received most attention due to their low cost, easy acquisition and good photo/chemical stability. Unfortunately, the widely used transition metal oxides like CeO_2, TiO_2 and ZnO can only exploit a small portion of solar light due to their wide bandgap,[4,5] and moreover the large excition binding energies of these semiconductors are unfavorable for separation of photogenerated electron and hole pairs.[6-8] Both disadvantages severely limit the practical application of transition metal oxides in photocatalytic water splitting. Generally, two strategies have been suggested to increase the solar energy utilization and enhance separation of the photoexcited electron and hole pairs. The first method involves doping of other metal ions into the transition metal oxide matrixes to narrow the band gap for harvesting more visible light; however, the metal dopants are likely to introduce deep impurity levels in the forbidden band of semiconductors, where they act as recombination centers and impair photocatalytic activity.[10,11] An alternative way is to create abundant surface defects on transition metal oxides, especially semiconductor nanomaterials of larger surface to bulk ratios, to improve separation efficiency of the electron and hole pairs.[13] Nevertheless, the control over both type and concentration of surface defects on semiconductor nanomaterials remains great challenge, causing that the impact of the surface defects on the photocatalytic activity is not clearly clarified.[14] Therefore, it is imperative to understand and manipulate the surface defects on transition metal oxide nanomaterials, which eventually benefits advancement of the photocatalysts toward efficient water splitting.

In this work, CeO_2 nanorods (NRs) of rather uniform size are chosen as the photocatalyst candidate for investigation of the influence of surface defects on the oxygen (O_2) evolution from water splitting. CeO_2 nanomaterials are well known to possess abundant surface oxygen vacancies (SOVs) as well as Ce^{3+} ions, which endow them many applications in CO oxidation[15,16], O_2 storage[17], solid oxide fuel cells[18], electrochemical water oxidation and high temperature organic oxidation[19]. Given the fact that CeO_2 nanomaterials themselves cannot efficiently utilize the visible light to split water due to the wide bandgap, such CeO_2 NRs would offer an excellent platform to study the effect of surface defects on water oxidation under visible light, when such defects are intentionally introduced. Furthermore, compared with the other half reaction of water splitting, the hydrogen (H_2) evolution, the O_2 evolution is a complicated four-electron process and represents more technical challenges.[6,20]

Synthesis of CeO_2 NRs starts from hydrothermal reaction of the solution containing the mixed $NH_3 \cdot H_2O$, ethanol and $CeCl_3 \cdot 7H_2O$. The morphology observation by scanning electron microscopy (SEM) and transmission electron microscopy (TEM) imaging shows that as-prepared products are rather uniform NRs with 1-3 μm in length and 40-100 nm in width (**Fig. 1a, 1b,** and **S1**). Powder X-ray diffraction (XRD) pattern reveals that the hydrothermal products are mixture of CeO_2, $Ce(OH)_3$ and Ce_2O_3 (**Fig. 1c**). Such a mixed composition is further proved by X-ray photoelectron

[a] Department of Physical Chemistry, School of Metallurgical and Ecological Engineering, University of Science and Technology Beijing, Beijing 100083, P. R. China. E-mail: ranboyu@ustb.edu.cn
[b] Key Laboratory of Nanosystem and Hierarchical Fabrication, , National Center for Nanoscience and Technology, Beijing 100190, P. R. China. Fax: (+86) 10-62656765. E-mail: zytang@nanoctr.cn, gaoyan@nanoctr.cn
[c] National Key Laboratory of Biochemical engineering, Institute of Process Engineering, Chinese Academy of Sciences, Beijing 100190, P. R. China.
Electronic Supplementary Information (ESI) available: [details of any supplementary information available should be included here]. See DOI: 10.1039/x0xx00000x

Journal of Material Chemistry A

COMMUNICATION

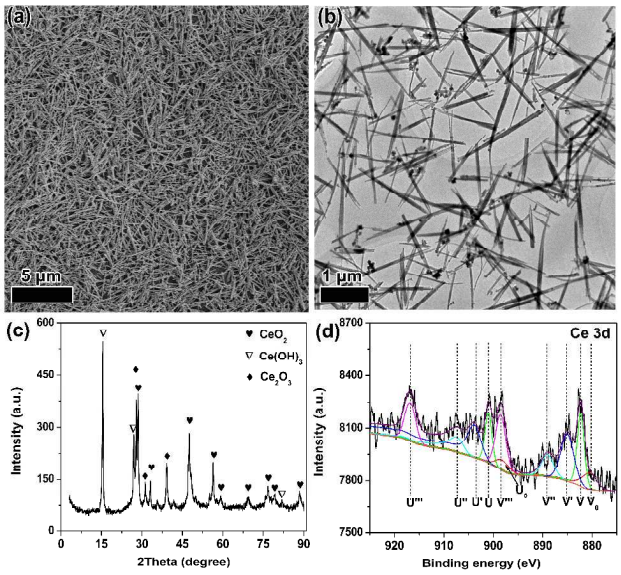

Fig. 1 (a) SEM image, (b) TEM image, and (c) XRD pattern of as synthesized Ce-based NRs; (d) corresponding XPS spectrum of Ce 3d. U''', V''', U'', V'', U, V, U', V', U_0 and V_0 represent the peaks of Ce^{4+} $3d_{5/2}$, Ce^{4+} $3d_{3/2}$, Ce^{4+} satellite, Ce^{4+} satellite, Ce^{4+} satellite, Ce^{4+} satellite, Ce^{3+} $3d_{5/2}$, Ce^{3+} $3d_{3/2}$, Ce^{3+} satellite and Ce^{3+} satellite, respectively.

spectroscopy (XPS) survey in which both Ce^{3+} and Ce^{4+} ions co-exist on the surface of the hydrothermal products **(Fig. 1d)**. In addition, the rich presence of the hydroxyl groups on the Ce-based NR surfaces can be also discerned by XPS analysis as well as transform infrared spectroscopy (FTIR) spectrum (**Fig. S2**).

Conversion of as-synthesized Ce-based composites to pure CeO_2 NRs has been performed by calcination at varying temperatures under different atmospheres including Ar mixed with 10% H_2 (in volume) (Ar-H_2), argon (Ar), and air (**Table S1**). The aim to implement the calcination process under different atmospheres is to introduce the surface defects of different densities into the products. Seen from the XRD pattern survey (**Fig. 2**), it is evident that when the calcination temperature is higher than 300°C and the calcination time is set to 3 h, all the Ce-based composites are completely converted to the surface modified CeO_2 NRs of the cubic fluorite structure regardless of the used atmospheres. In addition, the crystallinity of the calcinated products is found to be increased with raising the calcination temperature, and at the same calcination temperature the crystallinity of three CeO_2 NRs under Ar-H_2, Ar or air is almost same. Furthermore, all the calcinated products well preserve the original rod shape with identical size (**Fig. S3**). As comparison, when the calcination temperature is decreased to 100°C for 3 h, XRD data shows that partial Ce_2O_3 and $Ce(OH)_3$ are left in all the samples, demonstrating that high temperature benefits formation of CeO_2 phase (**Fig. S4**).

All as-calcinated samples shown in **Fig. 2** are then subjected to the UV-Vis diffuse reflectance spectroscopy (UV-Vis/DRS) characterization and visible-light stimulated O_2 evolution measurement (**Fig. S5** and **S6**). It is clear that though these samples obtained with same calcination temperature but different atmospheres have similar crystallinity, shape, size and surface area (**Fig. S7** and **Table S2**), they exhibit large difference in visible light absorption feature as well as O_2 evolution performance, especially for the samples treated at 800°C. This is understood that a high calcination temperature easily causes a large distinction in the surface defects of the samples under different atmospheres. Therefore, we select the CeO_2 NR samples treated at 800°C, named as Ar-H_2-800, Ar-800 and Air-800 as the representatives to disclose the effect of surface defects on the water oxidation under visible light.

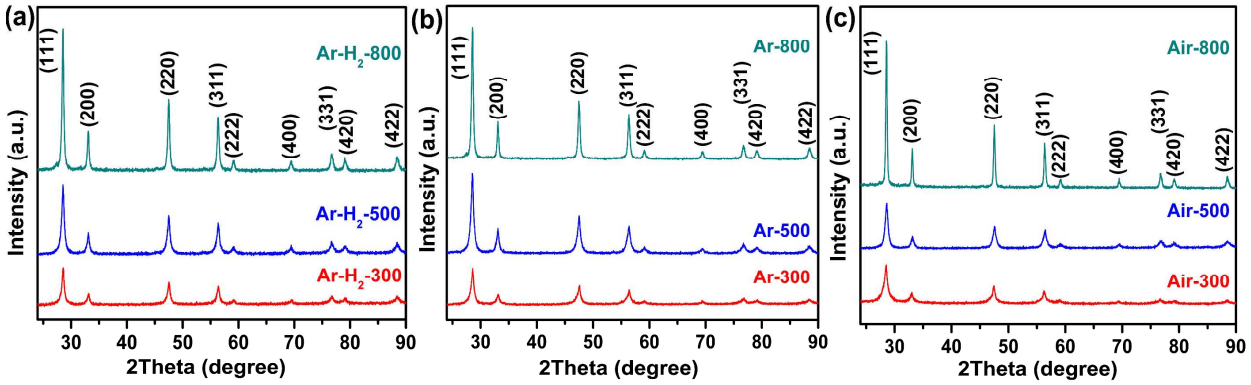

Fig. 2 (a), (b) and (c) XRD patterns of CeO_2 NRs calcinated under different atmospheres (Ar mixed with H_2 (10 % in volume), Ar, and air) at 300°C, 500°C and 800°C, respectively. The calcination duration for all the samples is set to 3 h.

Journal of Material Chemistry A

COMMUNICATION

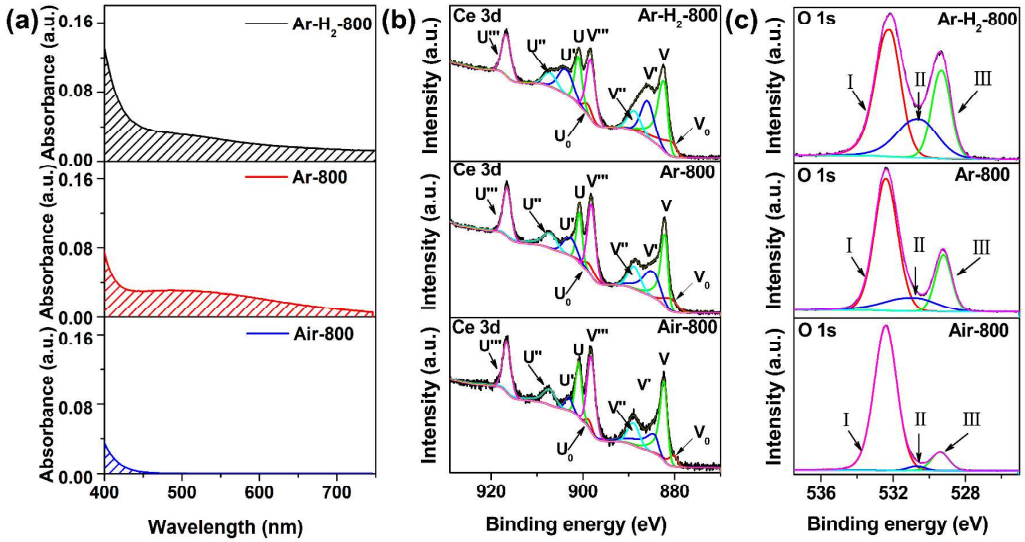

Fig. 3 (a) UV-Vis/DRS spectra of CeO_2 NRs calcinated at 800°C for 3 h under different atmospheres. (The shadowed areas display visible light absorption region.) (b) Ce 3d XPS spectra of Ar-H_2-800, Ar-800 and Air-800, respectively. U''', V''', U'', V'', U, V, U', V', U_0, V_0 represent the peaks of Ce^{4+} $3d_{5/2}$, Ce^{4+} $3d_{3/2}$, Ce^{4+} satellite, Ce^{4+} satellite, Ce^{4+} satellite, Ce^{4+} satellite, Ce^{3+} $3d_{5/2}$, Ce^{3+} $3d_{3/2}$, Ce^{3+} satellite and Ce^{3+} satellite, respectively. (c) O 1s XPS spectra of Ar-H_2-800, Ar-800 and Air-800 respectively; I, II and III stand for the peak of absorbed oxygen, active oxygen and lattice oxygen, respectively.

Among the surface defects, the SOVs of the calcinated products can be discerned by UV-Vis/DRS spectra (**Fig. 3a**). As displayed in **Fig. 3a**, the CeO_2 NRs treated with the mixed Ar and H_2 absorb maximum visible light in the wavelength region of 420 nm to 750 nm (black curve), whereas the CeO_2 NRs obtained with air treatment almost do not absorb any visible light (blue curve). Generally, SOVs would bring the defect energy levels between valence band and conduction band of the metal oxide semiconductors, resulting in the enhanced absorption in the range of visible light. Therefore, generating more SOVs in the CeO_2 NRs via thermal treatment with the mixed gas of Ar and H_2 should be reason to absorb more visible light. Furthermore, the appearance of SOVs is known to be associated with simultaneous formation of Ce^{3+} ions in CeO_2,[21,22] so the chemical composition difference in the products is investigated by XPS analysis (**Fig. 3b**). The surface of Ar-H_2-800 is of the highest ratio of Ce^{3+} (32.59%) corresponding to the peaks V_O, U_O, V' and U', compared with other two samples of Ar-800 (29.96%) and Air-800 (17.91%) (**Table S3)**. The similar difference in surface Ce^{3+} content is also recognized by electron paramagnetic resonance (EPR) spectra (**Fig. S8**).[25] Apparently, the fact that the surface of Ar-H_2-800 possesses more SOV and Ce^{3+} pairs than Ar-800 and Air-800 should be attributed to stronger chemical reduction under H_2 atmosphere at 800°C. Notably, the ratios of Ce^{3+} / (Ce^{3+} + Ce^{4+}) for the other products obtained at 300°C or 500°C follow the same trend (**Fig. S9**). We also notice from the O 1s XPS survey that three types of oxygen atoms coexist on the surface of post-treated CeO_2 NRs, and the peaks I, II and III are assigned to absorbed OH groups, active oxygen and lattice oxygen, respectively (**Fig. 3c**)**.** As demonstrated by **Table S3**, with respect to Ar-800 (15.51%) and Air-800 (2.05%), Ar-H_2-800 possesses a higher ratio of active oxygen (24.16%), which is reasonable because the active oxygen is closely bound to Ce^{3+} ion.[23,24]

Fig. 4a compares the O_2 yield using the three samples under irradiation with light of the wavelength over 420 nm. It is evident that the catalytic activity of Ar-H_2-800 is higher than that of Air-800 and Ar-800. Within 2 h, the O_2 yield from water oxidation is 67.68 μmol g^{-1} for Air-800, 642.84 μmol g^{-1} for Ar-800 and 707.73 μmol g^{-1} for Ar-H_2-800, respectively. Moreover, the photocatalytic performance of various CeO_2 NRs obtained with different atmospheres and temperatures is also systematically evaluated (**Fig. S6**), and Ar-H_2-800 exhibits the highest catalytic activity towards visible light water oxidization. Significantly, the initial rate of Ar-H_2-800 reaches 474.28 μmol g^{-1} h^{-1} (**Table S4**) and the average rate is up to 353.87 μmol g^{-1} h^{-1} for O_2 evolution under the visible light irradiation, which are comparable to the record value reported with transition metal oxides (**Table S5**).[26-28] Many control experiments have been performed to support the evidence that

Journal of Material Chemistry A

COMMUNICATION

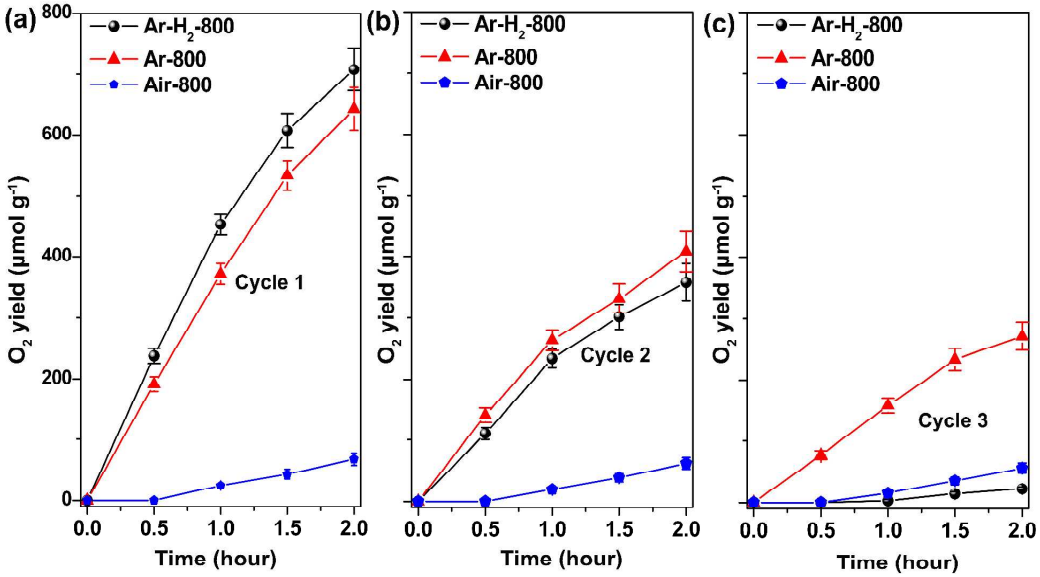

Fig. 4 (a) O_2 evolution as a function of reaction time over different catalysts under irradiation of visible light. (b) and (c) Plot of O_2 yield against irradiation time in the next two consecutive cycles. Reaction condition: total water volume, 75 mL; photocatalysts, 50.0 mg; $AgNO_3$, 0.01 M; light source, 300 W Xe lamp, λ ≥ 420 nm.

such O_2 evolution results from water oxidation catalyzed by Ar-H_2-800 under visible light irradiation (**Table S6**). It is also noticed that the photocatalytic performance of Ar-calcinated sample is considerably high and only slightly lower than that of Ar-H_2-calcinated sample at the same calcination temperature (382.26 μmol g^{-1} h^{-1} *vs.* 474.28 μmol g^{-1} h^{-1} in **Table S4**). Therefore, we exclude the possibility that hydrogen doped CeO_2 NR surfaces have the large contribution to enhancement of the water oxidation efficiency.

We also examined the photocatalytic durability of the corresponding samples by the repeated purge and injection cycles with an interval of 2 h. As shown in **Fig. 4b** and **4c**, with the cycle number increasing, the photocatalytic activity of all three samples shows the gradual decrease. It needs to be pointed out that as forAr-H_2-800, though its initial photocatalytic activity is the highest, the durability for water oxidation is the worst. The photocatalytic stability of different samples follows the below order: Air-800 > Ar-800 > Ar-H_2-800. The decreased activity could be understood from two aspects. On one hand, Ag nanoparticles, which are produced from sacrificial agent $AgNO_3$ after capture of photo-excited electrons, are deposited on the surface of CeO_2 NRs, and thus prohibit the photocatalytic reaction continuing.[27,29] The obviously high coverage of Ag nanoparticles on Ar-H_2-800 can be found by SEM images, TEM images and energy-dispersive X-ray(EDX) spectra (**Fig. S10** and **S11**). The prevention effect of Ag nanoparticles is further evidenced by choosing $Ce(NH_4)_2(NO_3)_6$ rather than $AgNO_3$ as the sacrificial agent, and all the samples are found to exhibit better durability (**Fig. S12**). On the other hand, the ratio of $Ce^{3+}/(Ce^{3+} + Ce^{4+})$ is decreased significantly during O_2 evolution process, especially for Ar-H_2-800 (**Fig. S13** and **Table S7**). This result can be understood that besides water oxidation for O_2 evolution, partial photogenerated holes might oxidize Ce^{3+} to Ce^{4+}, giving rise to the gradually decreased ratio of Ce^{3+} on CeO_2 NRs.[30]

How could formation of surface defects such as SOVs and Ce^{3+} ions in CeO_2 NRs lead to efficient O_2 evolution from water under visible light irradiation? To answer this question, the accurate energy level diagram of SOVs is firstly figured out based on investigation in combination of XPS valence band spectroscopy (XPS-VB), ultraviolet photoelectron spectroscopy (UPS) and UV-Vis/DRS (**Fig. 5**): (1) XPS-VB spectra of different samples calcinated at 800°C present three peaks, attributing to Ce 5s, O 2s and O 2p, respectively (**Fig. 5a**).[22] Detailed observation on O 2p XPS-VB peaks (the magnified images in **Fig. 5a)** reveals that the energy level position of the valence band maximum (VBM) is identical for all three products, around 2.4 eV below the Fermi level. (2) The accurate energy level position of the Fermi level might be estimated by UPS measurement (**Fig. 5b**). As for all the three samples, the energy difference between Fermi level and vacuum

Journal of Material Chemistry A

COMMUNICATION

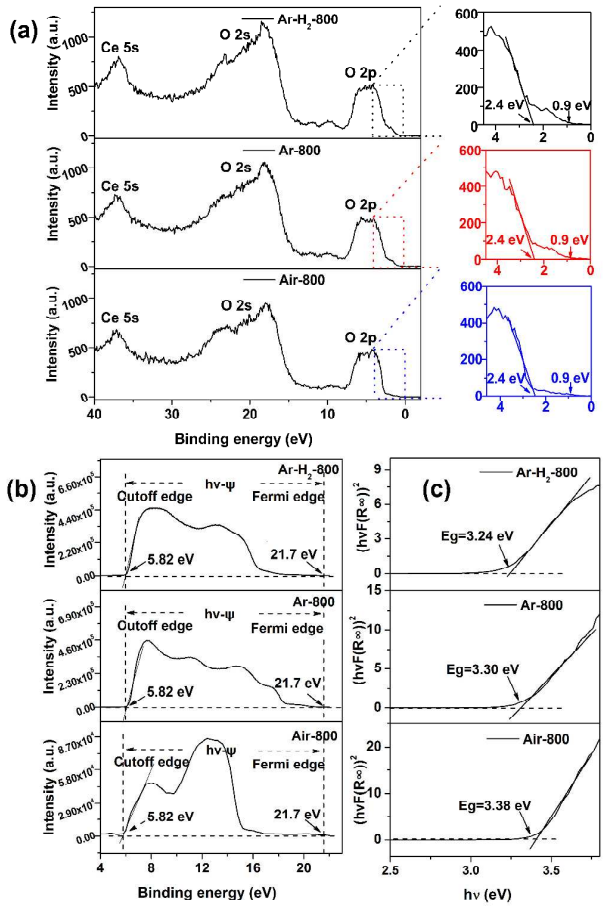

Fig. 5 (a) XPS-VB spectra of Ar-H_2-800, Ar-800 and Air-800. The magnified images of the selected area are O 2p XPS-VB spectra at 0 - 4.5 eV. (b) UPS profiles of Ar-H_2-800, Ar-800 and Air-800. (c) Band gap calculation of Ar-H_2-800, Ar-800 and Air-800 based on UV-Vis diffusion spectra.

energy is about 5.34 eV (**Fig. S14** and corresponding discussion). (3) Calculation on UV-Vis diffusion spectra indicates that all three samples have almost same band gap of 3.24 - 3.38 eV (**Fig. 5c**). Therefore, one can deduce that the position of the conduction band minimum (CBM) is ~0.8 eV above the Fermi level. (4) Finally, we also notice that there is obvious difference in the absorption intensity of O 2p XPS-VB spectra in the range of 0.9 to 2.4 eV, where Ar-H_2-800 and Air-800 exhibit the largest and smallest absorption intensity, respectively (inserts in **Fig. 5a**).[31] Such a difference in the absorption intensity is known to be caused by varied number of SOVs.[32-34] Accordingly, the energy level diagram of Ar-H_2-800 sample is drawn and shown in **Scheme 1a**. It is clear that most SOVs of the calcinated CeO_2 NRs are located near the VBM in the range of 7.74 eV to 6.24 eV, which is in good agreement with previous experimental and theoretical studies.[35,36] One can see from **Scheme 1a** that upon visible light illumination, the excited electrons from the defect states are transferred to the conduction band[36,37] and reduce the absorbed Ag^+ to Ag nanoparticles; meanwhile, the left excited holes in the SOVs would cause water oxidation to O_2. Evidently, generation of the SOVs on CeO_2 NRs should be critical for water oxidation under visible light. In order to further testify the effect of the SOVs, Xe lamp equipped with a cut filter of 500 nm (λ ≥ 500 nm) was used to assess the O_2 evolution performance. As shown in **Fig. S15**, there is no oxygen evolution with Air-800 as catalysts, whereas Ar-800 and Ar-H_2-800 of abundant SOVs might absorb more visible light (λ ≥ 500 nm) to produce considerable O_2. Except for photoexcited holes, the other key factor to influence O_2 evolution performance should be the catalytically active sites. As elucidated in the literatures,[38] water molecules are prone to absorb on the Ce^{3+} ions to be activated, which reduce the energy barrier to facilitate water oxidation (**Scheme 1b**). This catalytic role of the Ce^{3+} ions is also confirmed by repeated O_2 evolution experiment (**Fig. 4b** and**4c**). With water oxidation proceeding, partial Ce^{3+} ions are simultaneously oxidized to Ce^{4+} ions (**Fig. S13** and **Table S7**), resulting in the decrease of O_2 yield. Altogether, one can conclude that loss of O atoms on the CeO_2 NR surfaces at high temperature and under inert/reduced atmosphere gives rise to formation of Ce^{3+} and SOV pairs.[39] The rich SOVs effectively increase the visible light absorption as well as production of photogenerated holes, while Ce^{3+} sites adsorb water molecules and activate them. As a result, the holes trapped at SOVs react with the nearby water molecules adsorbed at Ce^{3+} ions to bring remarkable O_2 evolution.

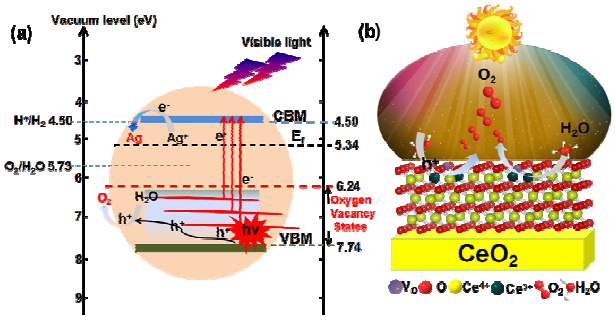

Scheme 1 (a) Energy level diagram of Ar-H_2-800, and its corresponding charge separation towards water oxidation under visible light illumination. (b) Schematic illustration of O_2 evolution on the surface defects of Ar-H_2-800.

Conclusion

We have demonstrated the superior photocatalytic activity of CeO_2 NRs for water oxidation under visible light irradiation, which outperforms the conventional WO_3, doped TiO_2 and CeO_2 modified with Au nanoparticles under visible light. Thanks to accurate acquisition of the energy level position of the SOVs and quantitative measurement of Ce^{3+} ions, we conclude that such exceptional photocatalytic activity of as-prepared CeO_2 NRs originates from synergetic effect of the SOVs and Ce^{3+} ions on their surfaces, which promotes absorption of visible light, generation of photoexcited holes and decrease of the energy barrier of water oxidation. More importantly, such surface defects like SOVs and Ce^{3+} ions are easily controlled by thermal treatment under various atmospheres. This finding not only gives the deep insight into the effect of surface defects of wide bandgap metal oxide nanomaterials on their physicochemical characteristics, but also provides the promising route for development of high-performance photocatalysts through manipulation of surface chemistry and physics.

Acknowledgements

This work was supported financially by National Key Basic Research Program of China (2014CB931801, Z.Y.T.), National Natural Science Foundation of China (21475029 and 91427302, Z.Y.T.; 51272047, Y.G.; 21271021 and 51472025 R.B.Y.), Instrument Developing Project of the Chinese Academy of Sciences (YZ201311, Z.Y.T.), CAS-CSIRO Cooperative Research Program (GJHZ1503, Z.Y.T.), and "Strategic Priority Research Program" of Chinese Academy of Sciences (XDA09040100, Z.Y.T.).

Notes and references

1 A. Kudo and Y. Miseki, *Chem. Soc. Rev*., 2009, **38**, 253–278; Y. B. Yan, J. W. Miao, Z. H. Yang, F. X. Xiao, H. B. Yang, B. Liu and Y. H. Yang, *Chem. Soc. Rev*., 2015, **44**, 3295–3346; G. Liu, L. Z. Wang, H. G.Yang, H. M. Cheng and G. Q. Lu, *J. Mater. Chem.*, 2010, **20**, 831–843.
2 X. Chen, S. Shen, L. Guo and S. S. Mao, *Chem. Rev*., 2010, **110**, 6503–6570; S. J. A. Moniz, S. A. Shevlin, D. J. Martin, Z. X. Guo and J. W. Tang, *Energy Environ. Sci.*, 2015, **8**, 731–759.
3 X. Ma, K. Zhao, H. J. Tang, Y. Chen, C. G. Lu, W. Liu, Y. Gao, H. J. Zhao and Z. Y. Tang, *Small*, 2014, **22**, 4664–4670; H. J. Yin and Z. Y. Tang, *Chem. Cat. Chem.*, 2015, **6**, 904–906.
4 R. Asahi, T. Morikawa, T. Ohwaki, K. Aoki and Y. Taga, *Science*, 2011, **293**, 269–271.
5 S. U. M. Khan, M. Al-Shahry and W. B. Ingler Jr., *Science*, 2002, **297**, 2243–2244; K. Zhao, J. Qi, S. L. Zhao, H. J. Tang, H. J. Yin, L. B. Zong, L. Chang, Y. Gao, R. B. Yu and Z. Y. Tang, *Chin. J. Catal.*, 2015, 36, 261-267.
6 J. Tang, J. R. Durrant and D. R. Klug, *J. Am. Chem. Soc*., 2006, **128**, 13885–13891.
7 W. Xie, Y. Li, W. Sun, J. Huang, H. Xie and X. Zhao, *J. Photochem. Photobiol. A: Chem.,* 2010, **216**, 149–155.
8 Y. Li, X. Zhou, X. Hu, X. Zhao and P. Fang, *J. Phys. Chem. C,* 2009, **113***,* 16188–16192.
9 P. Zawadzki, A. B. Laursen, K. Jacobsen, S. Dahl and J. Rossmeisla, *Energy Environ. Sci.*, 2012, **5**, 9866–9869.
10 M. Liu, X. Qiu, M. Miyauchi and K. Hashimoto, *J. Am. Chem. Soc.*, 2013, **135**, 10064–10072.
11 T. L. Thompson and J. T. Yates, *Chem. Rev*., 2006, **106**, 4428–4453; X. Chen and S. S. Mao, *Chem. Rev*., 2007, **107**, 2891-2959; S. T. Hoffmann, W. Y. Martin and D. W. Choi, *Chem. Rev*., 1995, **95**, 69–96.
12 X. Chen, L. Liu, P. Y. Yu and S. S. Mao., *Science*, 2011, **331**, 746–749.
13 M. Kong, Y. Li, X. Chen, T. Tian, P. Fang, F. Zheng and X. Zhao, *J. Am. Chem. Soc*., 2011, **133**, 16414–16417.
14 M. V. Ganduglia-Pirovano, J. Silva and J. Sauer, *Phys. Rev. Lett*., 2009, **102**, 026101.
15 C. Sun and D. Xue, *Phys. Chem. Chem. Phys.*, 2013, **15**, 14414–14419.
16 J. Qi**,** J. Chen**,** G. D. Li**,** S. X. Li**,** Y. Gao and Z. Y. Tang**,** *Energy Environ. Sci.*, 2012, **5**, 8937–8941.
17 S. Park, J. M. Vohs and R. J. Gorte, *Nature*, 2000, **404**, 265–267.
18 L. Chen, Y. Tang, L. Cui, C. Ouyang and S. Shi, *J. Power Sources*, 2013, **234**, 69–81.
19 J. M. Lopez, A. L. Gilbank, T. Garcia, B. Solsona, S. Agouram and L. Torrente-Murciano, *Appl. Catal., B: Environ.*, 2015, **174**, 403–412; F. L. Liang, Y. Yu, W. Zhou, X. Y. Xu and Z. H. Zhu, *J. Mater. Chem. A*, 2015, **3**, 634–640.
20 C. G. Silva, R. Juárez, T. Marino, R. Molinari and H. García, *J. Am. Chem. Soc.*, 2011, **133**, 595–602; Da. J. Martin, P. J. T. Reardon, S. J. A. Moniz and J. W. Tang, *J. Am. Chem. Soc.*, 2014, **136**, 12568−12571.
21 H. Li, H. Wang, X. Gong, Y. Guo, G. Lu and P. Hu, *Phys. Rev. B*, 2009, **79**, 193401.
22 N. V. Skorodumova, R. Ahuja, S. I. Simak, I. A. Abrikosov, B. Johansson and B. I. Lundqvist, *Phys. Rev. B*, 2001, **64**,115108.
23 D. A. Andersson, S. I. Simak, B. Johansson, I. A. Abrikosov and N. V. Skorodumova, *Phys. Rev. B*, 2007, **75**, 035109.
24 N. V. Skorodumova, S. I. Simak, B. I. Lundqvist, I. A. Abrikosov and B. Johansson, *Phys. Rev. Lett.*, 2002, **89**, 166601.
25 E. Abi-Aad, A. Bennani, J. P. Bonnelle and A. Aboukaïs, *J. Chem. Soc. Faraday Trans.*, 1995, **91**, 99–104; Z. Sojka and M. Che, *Appl. Magn. Reson.*2001, **20**, 433–456.
26 G. Liu, J. F. Han, X. Zhou, L. Huang, F. X. Zhang, X. L. Wang, C. M. Ding, X. J. Zheng, H. X. Han, C. Li, *J. Catal*., 2013, **307**, 148–152.
27 A. Primo, T. Marino, A. Corma, R. Molinari and H. García, *J. Am. Chem. Soc.*, 2011, **133,** 6930–6933.
28 C. Lavorato, A. Primo, R. Molinari and H. García, *ACS Catal*., 2014, **4**, 497–504; H. Kato and A. Kudo, *J. Phys. Chem. B*, 2002, **106***,* 5029–5034.
29 J. Qi, K. Zhao, G. Li, Y. Gao, H. Zhao, R. Yu and Z. Tang, *Nanoscale*, 2014, **6**, 4072–4077.
30 X. W. Liu, K. B. Zhou, L. Wang, B. Y. Wang and Yadong Li, *J. Am. Chem. Soc.*, 2009, **131**, 3140–3141.
31 A. Soultati, A. M. Douvas, D. G. Georgiadou, L. C. Palilis, T. Bein, J. M. Feckl, S. Gardelis, M. Fakis, S. Kennou, P. Falaras, T. Stergiopoulos, N. A. Stathopoulos, D. Davazoglou, P. Argitis and M. Vasilopoulou, *Adv. Energy Mater*., 2014, **4**, 1300896; F. X. Xie, W. C. H. Choy, C. D. Wang, X. C. Li , S. Q. Zhang and J. H. Hou, *Adv. Mater.*, 2013, **25**, 2051–2055; J. Gao, C. L. Perkins, J. M. Luther, M. C. Hanna, H. Y. Chen, O. E. Semonin, A. J. Nozik, Ra. J. Ellingson and M. C. Beard, *Nano Lett*. 2011, **11**, 3263–3266.
32 I. Nakamura, N. Negishi, S. Kutsuna, T. Ihara, S. Sugihara and K. Takeuchi, *J. Mol. Catal. A: Chem.*, 2000, **161**, 205–212.
33 X. Chen, L. Liu, Z. Liu, M. A. Marcus, W. Wang, N. A. Oyler, M. E. Grass, B. Mao, P. Glans, P. Y. Yu, J. Guo and S. S. Mao, *Sci. Rep.*, 2013, **3**, 1510.

34 P. Patsalas and S. Logothetidis, *Physical Review B*, 2003, 68, 035104; A. D. Liyanage, S. D. Perera, K. Tan,Y. Chabal and K. J. Balkus. Jr, *ACS Catal.* 2014, **4**, 577−584.
35 M. Huang and S. Fabris, *Phys Rev. B*, 2007, **75**, 081404.
36 S. Fabris, S. Gironcoli, S. Baroni, G. Vicario and G. Balducci, *Phys. Rev. B*, 2005, **71**, 041102.
37 S. Kundu, J. Ciston, S. D. Senanayake, D. A. Arena, E. Fujita, D. Stacchiola, La. Barrio, R. M. Navarro, J. L. G. Fierro and J. Rodrigue, *J. Phys. Chem. C*, 2012, **116**, 14062−14070.
38 D. Marrocchelli and B. Yildiz, *J. Phys. Chem. C*, 2012, **116**, 2411–2424; M. Fronzi, S. Piccinin, B. Delley, E. Travers and C. Stampfl, *Phys. Chem. Chem. Phys.*, 2009, **11**, 9188–9199; J. Paier, C. Penschke and J. Sauer, *Chem. Rev.*, 2013, **113**, 3949–3985.
39 F. Esch, S. Fabris, L. Zhou, T. Montini, C. Africh, P. Fornasiero, Comelli and R. Rosei, *Science*, 2005, **309**, 752–753; C. Ho, J. C. Yu, T. Kwong, A. C. Mak and S. Lai, *Chem. Mater*., 2005, **17**, 4514–4522.